Fracture modes in brittle coatings with large interlayer modulus mismatch

Herzl Chai[a)]
Department of Solid Mechanics, Materials and Structures, Faculty of Engineering,
Tel Aviv University, Israel 69978

Brian Lawn
Materials Science and Engineering Laboratory, National Institute of Standards and Technology,
Gaithersburg, Maryland 20899

Sataporn Wuttiphan
National Metal and Materials Technology Center, Bangkok 10400, Thailand

Fracture modes in a model glass–polymer coating–substrate system indented with hard spheres are investigated. The large modulus mismatch between the glass and polymer results in distinctive transverse fracture modes within the brittle coating: exaggerated circumferential (C) ring cracks that initiate at the upper coating surface well outside the contact (as opposed to the near-contact Hertzian cone fractures observed in monolithic brittle materials); median–radial (M) cracks that initiate at the lower surface (i.e., at the substrate interface) on median planes containing the contact axis. Bonding between the coating and substrate is sufficiently strong as to preclude delamination in our system. The transparency of the constituent materials usefully enables *in situ* identification and quantification of the two transverse fracture modes during contact. The morphologies of the cracks and the corresponding critical indentation loads for initiation are measured over a broad range of coating thicknesses (20 μm to 5.6 mm), on coatings with like surface flaw states, here ensured by a prebonding abrasion treatment. There is a well-defined, broad intermediate range where the indented coating responds more like a flexing plate than a Hertzian contact, and where the M and C cracks initiate in close correspondence with a simple critical stress criterion, i.e., when the maximum tensile stresses exceed the bulk strength of the (abraded) glass. In this intermediate range the M cracks generally form first—only when the flaws on the lower surface are removed (by etching) do the C cracks form first. Finite element modeling is used to evaluate the critical stresses at crack initiation and the surface locations of the crack origins. Departures from the critical stress condition occur at the extremes of very thick coatings (monolith limit) and very thin coatings (thin-film limit), where stress gradients over the flaw dimension are large. Implications of the results concerning practical coating systems are considered.

I. INTRODUCTION

Hard coatings on soft substrates are of technological importance for the protection they afford underlying substrates from extraneous contacts or impacts. Important examples include cutting tools, thermal barrier coatings, car windscreens, eye glasses, teeth, and dental restorations. In all these cases it is imperative to ensure that the coating–substrate interfaces are well-bonded, to avoid delamination failures. The coatings in such cases never-theless tend to be brittle and are subject to premature failure from transverse (through-thickness) cracking, as revealed most conspicuously in indentation tests with hard spheres.[1–11] The nature and mechanics of transverse coating fractures are not well understood, particularly in relation to key variables like coating thickness and coating–substrate modulus mismatch—failure modes can be especially complex in thicker coatings with large mismatch.[8,11] Detailed experimental observations on contact failure modes are sparse, with observations of the fracture patterns generally restricted to *a posteri* examinations. Several finite element model (FEM) stress analyses

---

of such modes in layer structures have been report-ed,[12–17] mostly on very thin films, but usually without systematic investigation of key variables and often with-out any detailed experimental confirmation.

In this paper we investigate the fracture modes in a model glass–polymer coating–substrate system indented with hard spheres. Specifically, we use glass coatings 20 μm to 5.6 mm thick, with tungsten carbide sphere indenters 3.96 mm radius. This particular material–indenter system is chosen for three reasons. (i) The constituent bilayer materials are transparent, enabling *in situ* observation of crack accumulation and evolu-tion within the brittle coating during contact. (ii) The coating thickness can be easily varied and controlled within a broad range. (iii) The interlayer modulus mismatch is large, favoring the incidence of crack systems other than the conventional near-contact Hertzian cone cracks that initiate in monolithic brittle materials.[18–23] We describe the morphological evolution of two distinctive coating crack systems during the con-tact loading: top surface circumferential ring cracks that initiate well outside the contact circle; subsurface median–radial cracks that initiate at the substrate inter-face. The subsurface radial cracks are of special interest, because it is sometimes assumed (based on postmortem examination of cracks in opaque material systems) that they must initiate from the top surface[16]—we confirm that this is not so, at least for "blunt" spherical indenters and soft substrates of interest here. At small thicknesses the subsurface cracks are somewhat inhibited in their growth, and the ring cracks once more form close to the contact circle.

To place the observations on a quantitative footing, we measure the critical indentation loads for the initiation of the surface circumferential and subsurface median–radial cracks as a function of coating thickness. For coatings in an intermediate range of thickness (50 μm ≲ d ≲ 2 mm) the critical loads for outer circumferential cracks and median–radial cracks are consistent with predictions from FEM analyses based on initiation when the maxi-mum tensile stresses exceed the bulk strength of the glass. On the other hand, a simple critical stress condition is inadequate for predicting the initiation of near-contact circumferential cracks in the extremes of very small (thin-film limit) or very large (monolith limit) coating thicknesses.

II. EXPERIMENTAL PROCEDURE

We construct a model material coating–substrate system to enable direct *in situ* viewing of coating frac-ture during indentation testing, Fig. 1. For this purpose we choose two transparent materials, soda-lime glass as the coating and polycarbonate polymer as the substr-ate. The soda-lime glass is ideally hard and brittle; the
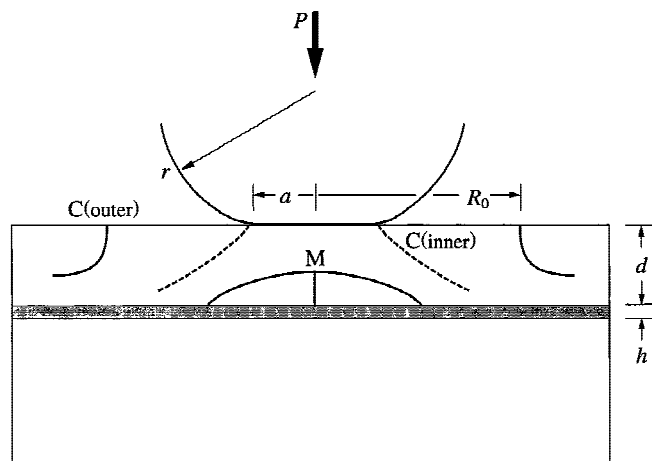

FIG. 1. Schematic of transverse cracks in stiff coating on compliant substrate, showing indenter of radius r at load P on coating of thick-ness d bonded to substrate with adhesive of thickness h. Surface cir-cumferential outer and inner C cracks form at radius R_0 around the contact circle, radius a. Subsurface median–radial M cracks form at coating–substrate interface.

polycarbonate is relatively soft and nonbrittle with little viscous component, thus minimizing rate effects in the deformation.

Soda-lime window glass plates 75 × 25 × 5.6 mm (Gaithersburg Glass, Gaithersburg, MD) were ground to prescribed thicknesses within the range d = 20 μm to 5.6 mm and polished to 1 μm diamond paste. Chemi-cal etching in a solution of 12% HF acid was also useful as a means of thinning at the lower end of the thickness range. In order to obtain reproducible data se-lective abrasion of the glass surfaces was employed,[24] using a slurry of 600 SiC grit. In some specimens both the upper and lower plate surfaces were abraded, to introduce a uniform density of controlled flaws for the subsequent fracture tests. In other specimens only the upper or lower surfaces were abraded and the oppo-site surfaces etched in 12% HF solution for 10 min to provide an effectively flaw-free finish. In yet other specimens both surfaces were left in their as-polished states, to determine the response of natural flaw distri-butions. An epoxy adhesive (Harcos Chemicals, Belles-ville, NJ) was used to bond the lower glass surface to the upper surface of a smoothly finished polycarbonate slab (AIN Plastics, Norfolk, VA) 75 × 25 × 12.70 mm, under light pressure. The thickness of the final adhesive layer was h = 20–30 μm in most specimens. A few specimens were constructed with adhesive layers h ≈ 300 μm thick, to check for any spurious effects of interlayer bond thickness.

Indentation tests were conducted on the upper glass surfaces with tungsten carbide (WC) spheres of radius r = 3.96 mm, in a screw-driven testing machine (Instron 4501, Instron Corp, Canton, MA). These tests were made

in air, at crosshead speeds such that cracks initiate in the glass coatings within 1 min or so. The subsurface contact regions in the coatings were observed *in situ* using a Questar telescope (Questar, New Hope, PA), either directly through the side surface or from below using a half-mirror to redirect the light source; in the latter case the upper (contact) surface was precoated with a gold film to enhance reflection. The indentation crack evolution was monitored on a video recorder. Critical loads to initiate each fracture mode were measured as a function of coating thickness. Some specimens were sectioned *a posteri* through the indentation sites and viewed in transmitted light.

Some subsidiary tests were conducted to provide essential material characterization data for later analysis:

(*i*) *Indentation stress–strain curves.* Indentation stress ($p_0 = P/\pi a^2$) was measured as a function of indentation strain (a/r) for bulk glass and polycarbonate polymer specimens, with P load and a contact radius (Fig. 1).[25–27] These tests were made at the same loading rates as in the contact damage tests described above.

(*ii*) *Bulk strengths.* Strengths σ_F of abraded glass slabs $75 \times 19 \times 5.6$ mm with chamfered edges (to avoid edge failures) were measured in four-point flexure (inner span 27 mm and outer span 61 mm).

III. RESULTS

A. Crack morphology

Figures 2–5 show coating fracture evolution with sequentially increasing contact load P in glass–polycarbonate specimens at selected coating thicknesses d, for specified glass surface flaw states, photographed *in situ* from below the contact during loading. These four sequences are chosen as representative of the different crack patterns observed within an "intermediate" thickness range (quantified in Sec. III. B, below). In these sequences we identify subsurface-initiated median–radial M cracks and surface-initiated "inner" and "outer" circumferential C cracks. The source of initiation, upper or lower surface, is determined by side-on viewing. Abrasion flaws are clearly visible in the photographs.

Figure 2: d = 230 μm, upper and lower surfaces both abraded. (a) M cracks initiate within the coating from the lower surface (i.e., from the interface with the substrate) on median planes normal to the specimen surface and containing the contact axis. (b) As the load increases, more M cracks pop in, one at a time at angles approximately bisecting two nearest-neighbor predecessors, and extend radially. (c) M cracks continue to initiate and extend. (d) An inner C crack initiates close
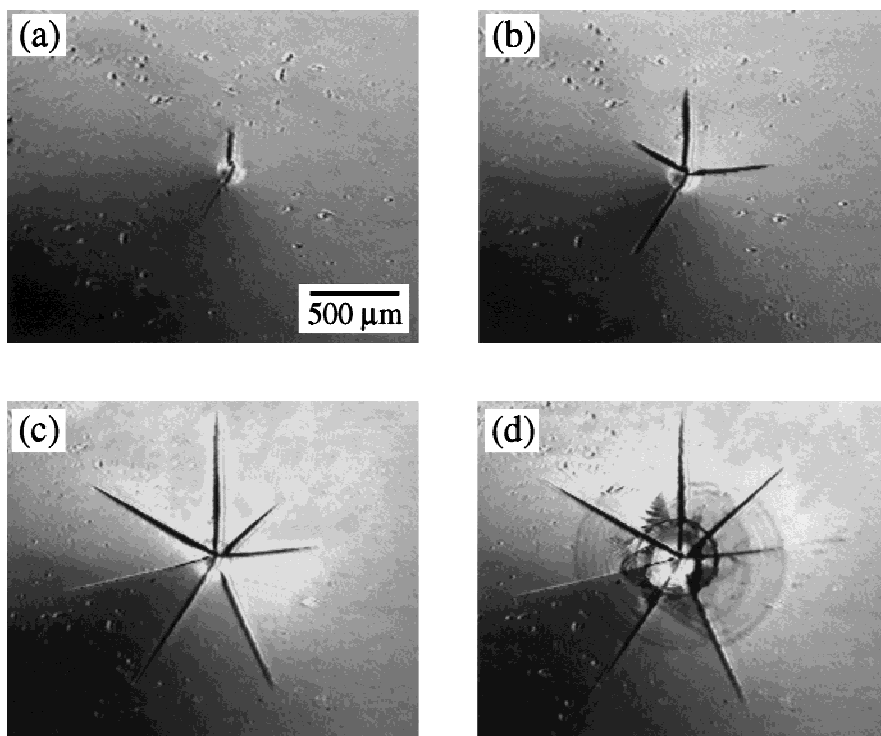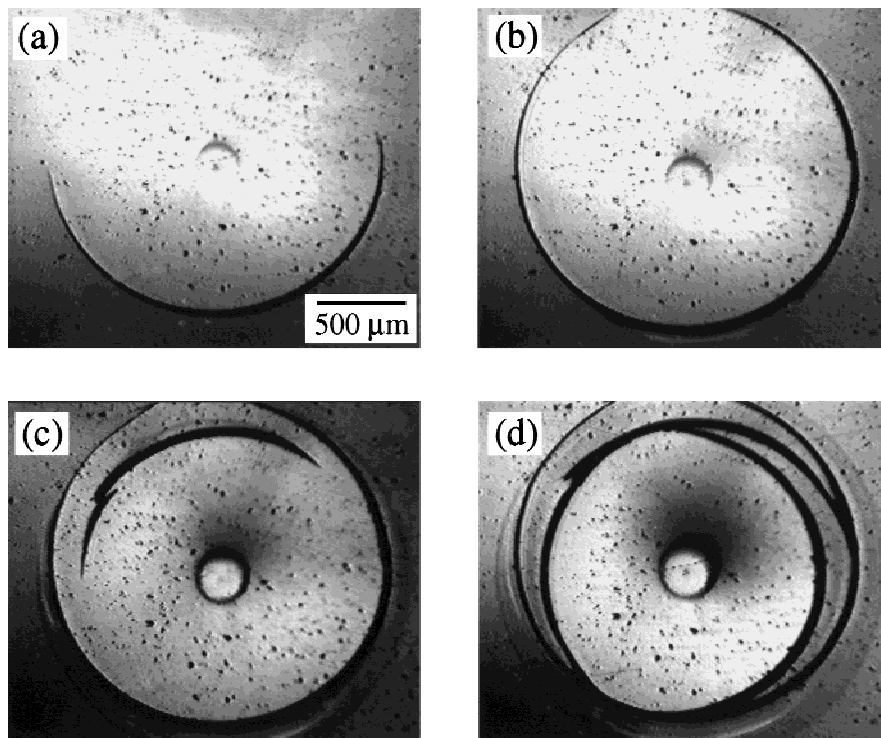

FIG. 2. *In situ* sequence of coating crack evolution in soda-lime glass coatings on polycarbonate polymer substrates, WC indenter radius $r = 3.96$ mm and coating thickness $d = 230$ μm, both upper and lower surfaces abraded: (a) $P = 9.0$ N, $a = 89$ μm; (b) $P = 15.4$ N, $a = 106$ μm; (c) $P = 31.2$ N, $a = 136$ μm; (d) $P = 36.0$ N, $a = 145$ μm. Median–radial M cracks precede inner circumferential C cone cracks (note Fizeau fringes at open cone interface). Abrasion flaws are visible.

FIG. 3. *In situ* sequence of coating crack evolution in soda-lime glass coating on polycarbonate polymer substrate, WC indenter radius $r = 3.96$ mm and coating thickness $d = 230$ μm, upper surface abraded, lower surface etched: (a) $P = 66.7$ N, $a = 194$ μm; (b) $P = 67.0$ N, $a = 195$ μm; (c) $P = 103$ N, $a = 230$ μm; (d) $P = 104$ N, $a = 231$ μm. Only outer circumferential C cracks formed. Abrasion flaws on top surface are visible.
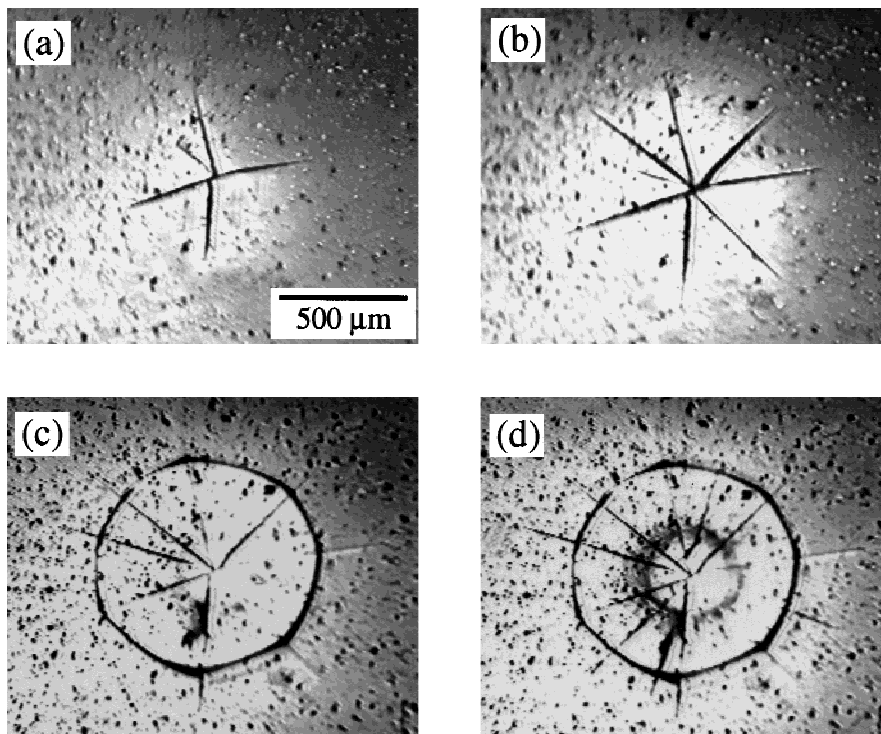

FIG. 4. *In situ* sequence of coating crack evolution in soda-lime glass coating on polycarbonate polymer substrate, WC indenter radius $r = 3.96$ mm and coating thickness $d = 140$ μm, both upper and lower surfaces abraded: (a) $P = 11.3$ N, $a = 98$ μm; (b) $P = 16.0$ N, $a = 118$ μm; (c) $P = 23.8$ N, $a = 153$ μm; (d) $P = 27.0$ N, $a = 162$ μm. Sequence is similar to that of Fig. 2, but circumferential C cracks now form well outside contact. Abrasion flaws are visible.
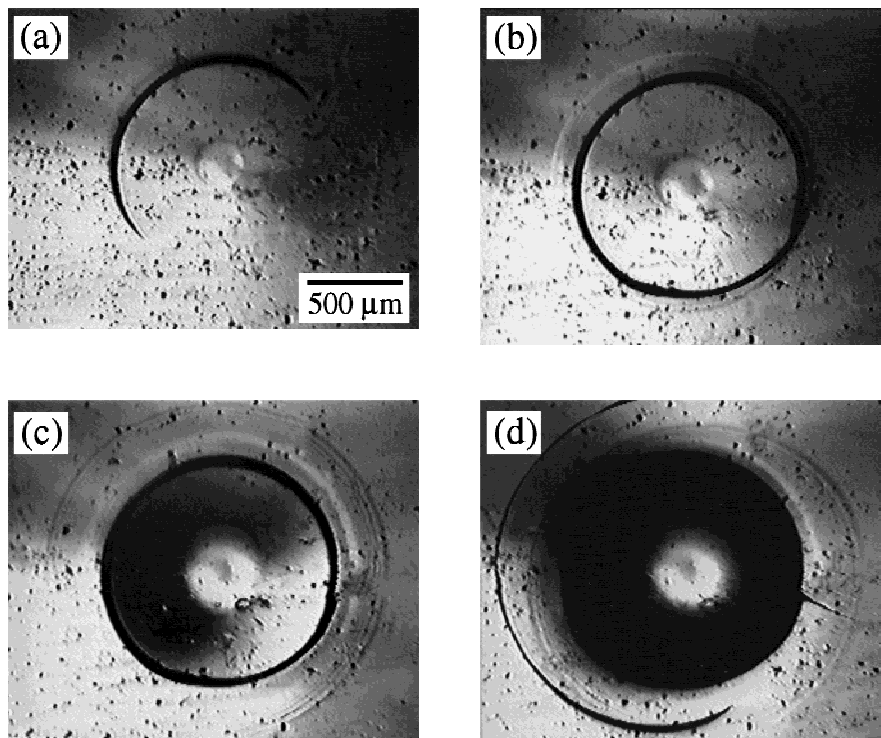
FIG. 5. *In situ* sequence of coating crack evolution in soda-lime glass coating on polycarbonate polymer substrate, WC indenter radius $r = 3.96$ mm and coating thickness $d = 140$ µm, upper surface abraded, lower surface etched: (a) $P = 28.6$ N, $a = 163$ µm; (b) $P = 35.0$ N, $a = 186$ µm; (c) $P = 70.0$ N, $a = 256$ µm; (d) $P = 140$ N, $a = 265$ µm. Cf. Fig. 3; only outer circumferential C cracks are formed. Abrasion flaws on top surface are visible.

to the contact circle (central bright spot) and grows downward and outward within the coating into a Hertz-like cone configuration.

Figure 3: $d = 230$ µm, upper surface abraded, lower surface etched. (a) An outer C crack initiates into an arc from a flaw at the coating upper surface, well outside the contact circle. (b) The C crack runs around the contact and completes itself into a near-axisymmetric surface ring. (c) At higher load a second, near-concentric C crack initiates within the first, but still far outside the contact. (d) The surface ring cracks propagate downward and outward within the coating. No M cracks are observed with further increase in load.

Figure 4: $d = 140$ µm, upper and lower surfaces both abraded, (a) M cracks initiate from below and extend and (b) proliferate. (c) At somewhat higher load, an outer C crack initiates at the upper surface well outside the contact near the extremities of the preceding M cracks. (d) With further slight increase in load, an inner C crack initiates, similarly to that in Fig. 2(d).

Figure 5: $d = 140$ µm, upper surface abraded, lower surface etched. (a) A C crack initiates, (b) completes itself, and (c) propagates downward and outward. (Note that the size of this crack is comparable to that in Fig. 4.) (d) At higher load, additional C cracks initiate. (Again, no M cracks are observed at higher loads.)

These four sequences provide interesting comparisons and contrasts at the different (intermediate) coating thicknesses and surface flaw states. If just the upper surface is abraded and the lower surface etched, only outer C cracks form, regardless of d (Figs. 3 and 5). If both the upper and lower surfaces are abraded the M cracks form first, again regardless of d (Figs. 2 and 4). In this latter case, however, the configurations of the secondary C cracks that form *after* the M cracks *are* dependent on d: at $d = 230$ µm (Fig. 2) only inner C cracks form, whereas at $d = 140$ µm (Fig. 4) both outer and inner C cracks form. Note that the C cracks appear segmented between the radial cracks in Fig. 4, indicating strong crack–crack interactions.

Figure 6 shows analogous *in situ* micrographs of the crack patterns at the extremes of (a) "large" thickness, $d = 5.6$ mm, and (b) "small" thickness, $d = 42.5$ µm, at loads substantially above critical, in coatings with only upper surfaces abraded. At $d = 5.6$ mm only an inner C crack forms, just outside the contact circle, in the traditional manner of Hertzian cone cracks in brittle monoliths.[21,23,28] At $d = 42.5$ µm faint, concentric shallow ring cracks are observed around the contact.[29] Direct *in situ* viewing at increasing load confirms a multiplicity of ring crack initiation outside the ever-expanding contacts in both the thin and thick coatings.

The profile morphologies of the C cracks are revealed more clearly in section views. Such views are shown in Fig. 7, at $d = 390$ μm with (a) both surfaces abraded and (b) only upper surface abraded (lower surface etched), at loads well above critical. These micrographs confirm that the C cracks initiate from the upper surface. In neither case does the crack penetrate through the lower surface of the coating, preferring to deflect nearly parallel to the substrate interface. Nonetheless, a basic difference between the inner C crack in Fig. 7(a) and outer C crack in Fig. 7(b) is manifest: the former assumes more the familiar cone geometry but with an upturned "brim" at its edge[30] [note the trace of an M crack along the contact axis in Fig. 7(a), partly obscured by the cone]; the latter

extends initially deeper and subsequently deflects horizontally at approximately a quarter layer thickness from the interface.

Figure 8 is an *in situ* side view of two radial arms of an M crack at $d = 1.0$ mm. In this case the micrograph confirms initiation from the lower coating surface. Indeed, the crack remains entirely confined subsurface in its subsequent propagation—in some specimens the M cracks were observed to extend laterally to the edges of the specimen, a distance greater than 10–20 mm, without ever reaching the upper surface.

FIG. 7. Section views of C cracks in soda-lime glass coatings on polycarbonate polymer substrates, $d = 390$ μm and WC indenter radius $r = 3.96$ mm: (a) both upper and lower surfaces abraded, showing inner C crack, $P = 75$ N; (b) only upper surface abraded, showing outer C crack, $P = 275$ N.
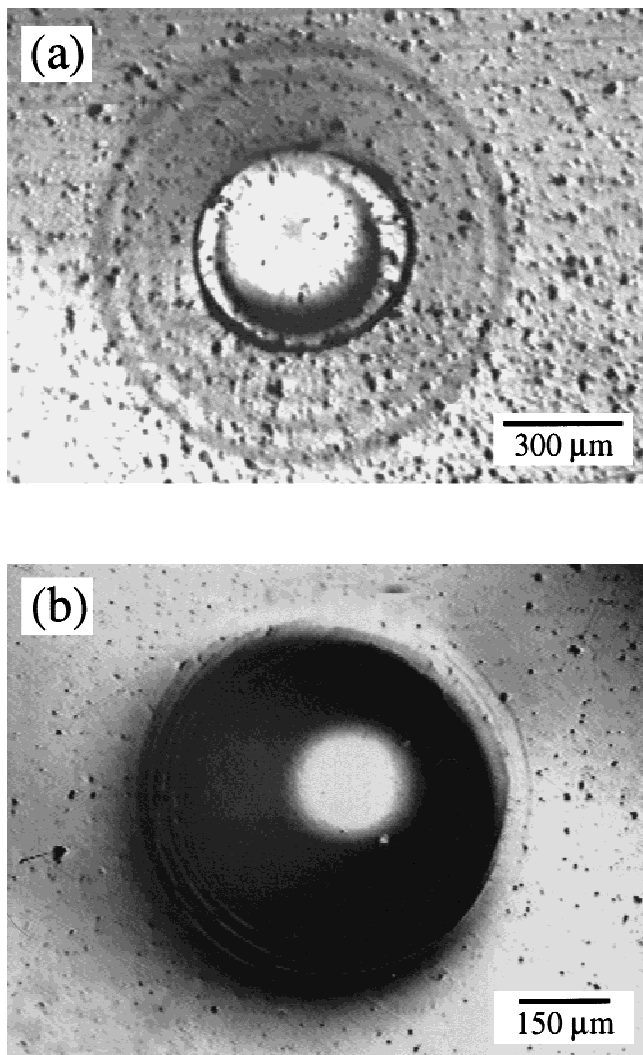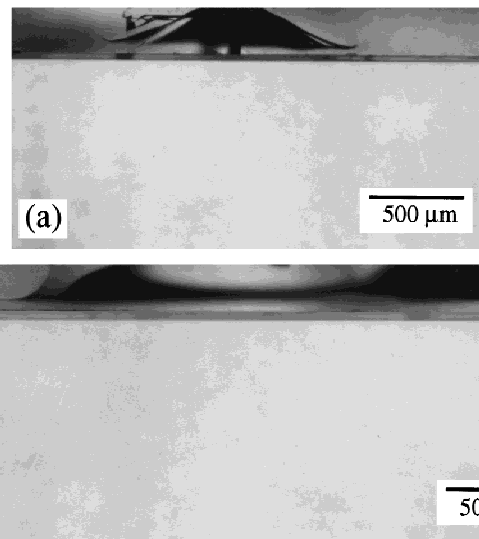

FIG. 6. *In situ* micrographs of cracks in soda-lime glass coatings on polycarbonate polymer substrates, both upper and lower coating surfaces abraded, WC indenter radius $r = 3.96$ mm: (a) $d = 5.6$ mm, $P = 392$ N, $a = 226$ μm, inner Hertzian C crack; (b) $d = 42.5$ μm, $P = 116$ N, $a = 335$ μm, faint traces of inner C cracks visible.
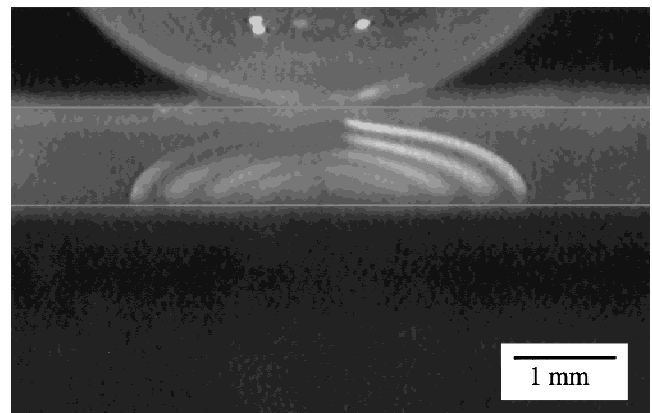

FIG. 8. Side view of M crack in soda-lime glass coating on polycarbonate polymer substrate, $d = 1.0$ mm, WC indenter radius $r = 3.96$ mm, and $P = 130$ N, both upper and lower surfaces abraded (note Fizeau fringes). Crack extends laterally but remain wholly contained below the upper coating surface. (Top coating surface and coating–substrate interface artificially highlighted for clarity.)

A compelling feature of the morphological observations is a certain geometrical similarity of the transverse M and C cracks. Each crack system is observed to have a nearly invariant geometry relative to the coating thickness over the intermediate range of *d*. Another compelling feature is the high degree of crack stability. The M and C cracks extend and proliferate with load and ultimately intersect each other, yet do not easily penetrate through the coating thickness. Considerable load increase beyond the first initiation load is required to cause general coating failure.

No delamination cracks were observed in our system over the load ranges covered.

B. Critical loads for cracking modes

Figure 9 plots critical load P_c for the onset of surface circumferential C cracks and subsurface median–radial M cracks as a function of coating thickness *d,* for specimens with just one surface abraded and opposite surface etched, and for specimens with both upper and lower glass surfaces abraded. Figure 10 plots corresponding surface radius R_0, normalized to contact radius *a* (Fig. 1), as a function of *d* for the C cracks. Data points in these figures are experimental observations. Circles represent C cracks, diamonds M cracks; filled symbols represent

first-fracture events, unfilled symbols subsequent-fracture events. Solid curves are predictions for first fracture from FEM analysis (see Sec. IV).

The data in Figs. 9 and 10 quantify the distinct regions of behavior alluded to in Sec. III. A above. We consider each of these regions below, taking the intermediate region of greatest interest first:

(*i*) *Intermediate thicknesses* (50 μm ≲ *d* ≲ 2 mm). For any specimens with abraded lower surfaces the M cracks form first (Figs. 2 and 4) and accordingly constitute the primary fracture mode. The critical loads P_c for the M cracks within this region decline monotonically with decreasing thickness *d* in Fig. 9 according to an empirical best-fit dependence $P_c \propto d^{1.75}$ (not plotted).

Formation of the C cracks occurs at higher critical loads within this region, by an amount dependent on the surface flaw states. For specimens with both upper and lower surfaces abraded the C cracks form after the M cracks (cf. Figs. 2 and 4). In these specimens, the ratio $P_c(C)/P_c(M)$ diminishes as *d* increases (open circles, Fig. 9), approaching unity at the upper end of this thickness range. The corresponding thickness dependence of C-crack surface radius to contact radius, R_0/a, is complex (Fig. 10): At *d* ≈ 50 μm, the cracks form close to the contact circle, i.e., $R_0/a \approx 1$; as *d* increases, R_0/a di-
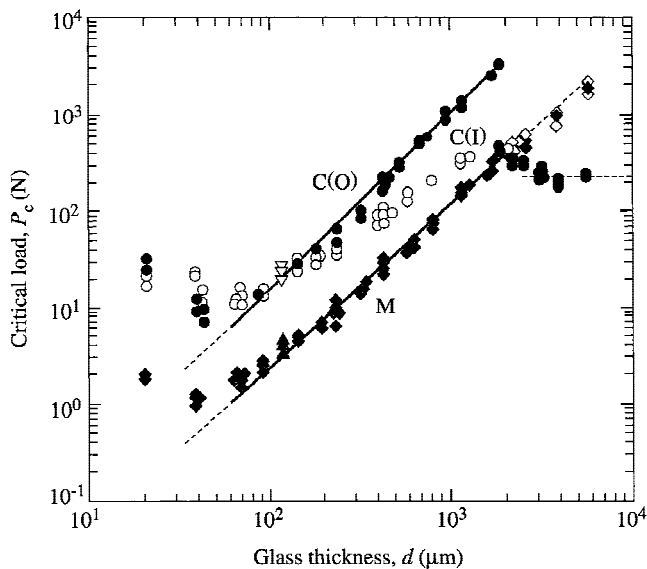
FIG. 9. Critical loads P_c to initiate M and C (outer O, inner I) cracks in soda-lime glass coatings on polycarbonate polymer substrates, as function of glass thickness *d*, with WC indenter radius *r* = 3.96 mm. Filled symbols are first-fracture experimental data for specimens with just upper or lower surfaces abraded and opposite surfaces etched. Unfilled symbols are subsequent-fracture experimental data for specimens with both upper and lower glass surfaces abraded. Circles are data for C cracks, diamonds for M cracks, for specimens with adhesive thickness *h* = 20–30 μm; triangles are data for comparative specimens with *h* ≈ 300 μm. Solid curves are FEM predictions, assuming initiation when the maximum tensile stress attains the strength of the bulk glass.
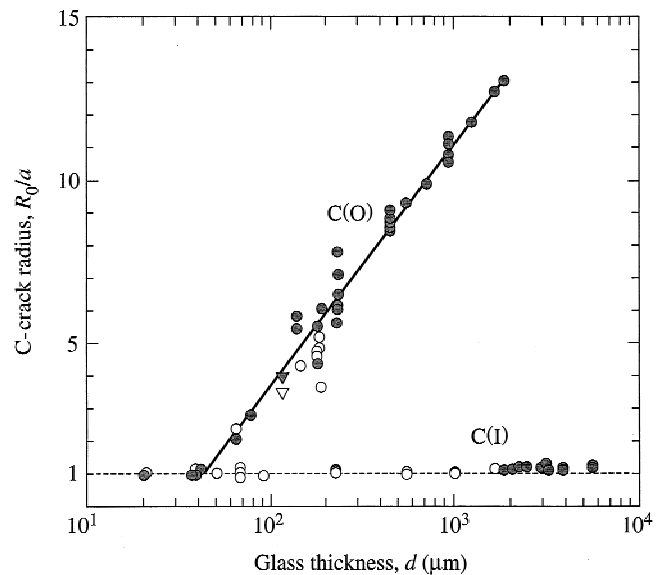
FIG. 10. Surface crack radius R_0 normalized to contact radius *a* for C (outer O, inner I; see Fig. 1) cracks in soda-lime glass coatings on polycarbonate polymer, as function of glass thickness *d,* with WC indenter radius *r* = 3.96 mm. Filled symbols are first-fracture experimental data for specimens with just upper or lower surfaces abraded and opposite surfaces etched. Unfilled symbols are subsequent-fracture experimental data for specimens with both upper and lower glass surfaces abraded. Circles are data for C cracks for specimens with adhesive thickness *h* = 20–30 μm; triangles are data for comparative specimens with *h* ≈ 300 μm. Solid curve is FEM prediction, from evaluations of locations of tensile stress maxima outside contact circle.

verges, corresponding to virtually simultaneous formation of inner (I) and outer (O) ring cracks, with $R_0(I)/a \approx 1$ but with rapid increase in $R_0(O)/a$, until, at $d \gtrsim 200$ μm, only inner C-cracks initiate, with $R_0/a \approx 1$ everywhere. For specimens with only upper surface abraded and lower surface etched (cf. Figs. 3 and 5), so that the M cracks are suppressed, $P_c(C)$ increases without discontinuity over the entire intermediate thickness range, with value of $R_0(O)/a$ in excess of 10 at $d \approx 2$ mm.

(*ii*) *Large thicknesses* ($d \gtrsim 2$ mm). For all specimens with upper surfaces abraded, conelike C cracks form first [cf. Fig. 6(a)], i.e., $P_c(C) < P_c(M)$, with surface rings at $R_0/a \approx 1.0$ to 1.2, as in monolithic brittle solids.[22,28] For specimens with both surfaces abraded secondary M cracks initiate at higher loads. Within this thickness region, $P_c(C)$ gradually increases and $P_c(M)$ decreases (consistent with extrapolation of the P_c–d curve from the intermediate region), as the coating thickness diminishes toward $d \approx 2$ mm, at which point the two types initiate virtually simultaneously.

For specimens with both surfaces abraded there appears to be a relatively smooth transition in R_0/a values between $d \gtrsim 2$ mm and $d \lesssim 2$ mm. However, for specimens with only upper surfaces abraded the corresponding transition in R_0/a is abrupt, indicating a sudden shift in location of maximum surface stress intensity from the near-contact to the far-contact region. For specimens with only lower surfaces abraded, M cracks form first, at about the same loads as for specimens with top surfaces also abraded. In this last case C cracks follow almost immediately.

(*iii*) *Small thicknesses* ($d < 50$ μm). The C and M cracks form in the same loading sequence as at $d \lesssim 200$ μm in region (i) but now at increasingly higher loads as d becomes smaller, so that extrapolations of the P_c–d curves from the intermediate region are no longer valid. C cracks once more form close to the contact circle [Fig. 6(b)].

C. Subsidiary tests

Comparative measurements of critical loads on specimens with both upper and lower surfaces in the as-polished states demonstrate the effect of flaw size and distribution. Figure 11 shows a Weibull plot of P_c for M-crack initiation in glass coatings of thickness $d = 230$ μm, along with corresponding data for specimens with lower surfaces abraded. The P_c data and, more importantly, their scatter are markedly higher for the unabraded surfaces, attesting to the role of flaw statistics.

Other critical-load tests on specimens with different adhesive thicknesses h indicate a relative insensitivity to interlayer dimension in our material system. Crack initiation data on glass coatings $d = 115$ μm with $h \approx 300$ μm instead of $h = 20$–30 μm in the control specimens are plotted as triangles in Figs. 9 and 10. The fact that

these data follow the same trend as the controls suggests that the epoxy adhesive may be considered as effectively part of the polycarbonate substrate.

Figure 12 shows indentation stress–strain curves for the constituent soda-lime and polycarbonate polymer materials, as input for FEM analysis (Sec. IV). Again, data points are experimental measurements and solid curves are theoretical fits. Nonlinearity is observed in the polycarbonate data.
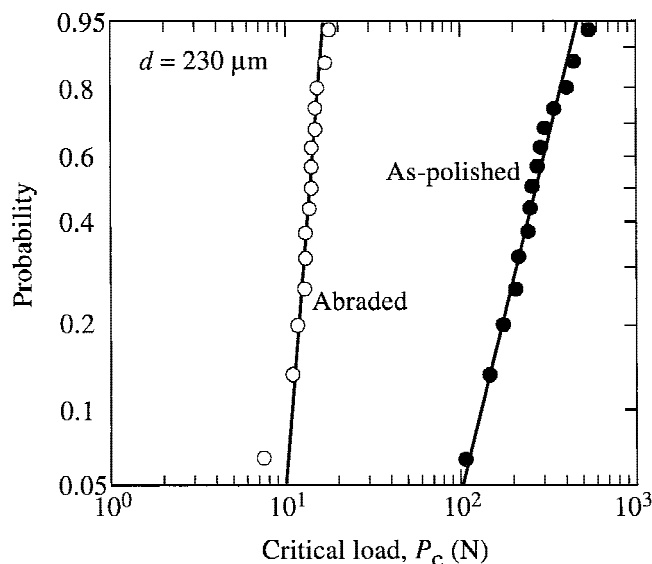

FIG. 11. Weibull plot of critical load to initiate M cracks, for soda-lime glass coatings of thickness $d = 230$ μm on polycarbonate substrates, with WC indenter radius $r = 3.96$ mm, comparing data for abraded and as-polished lower surfaces.
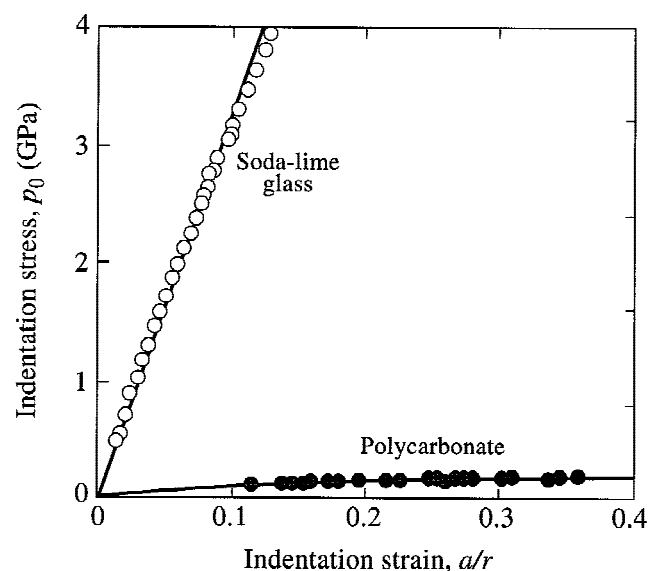

FIG. 12. Indentation stress–strain curves for bulk soda-lime glass and polycarbonate polymer materials, using WC spheres. Data points are experimental observations, and solid curves are FEM fits.

Measurements of bulk strengths of abraded glass flexure bars yield $\sigma_F = 110 \pm 5$ MPa. In conjunction with the Griffith strength relation $\sigma_F = \pi^{1/2}T_0/2c_f^{1/2}$ for pennylike flaws, using an effective toughness $T_0 = K_{IC} = 0.4$ MPa m$^{1/2}$ for soda-lime glass in the presence of moisture,[5] we evaluate a flaw size $c_f = 10 \pm 1$ μm.

IV. STRESS ANALYSIS

We use FEM to calculate the maximum tensile stresses in the glass coatings at the upper and lower surfaces, where the C and M cracks initiate. The algorithm for the computations has been described in detail elsewhere.[6,31,32] The computation assumes a sphere of radius $r = 3.96$ mm in frictionless contact with a flat bilayer system, with a minimum grid size 3 μm in the critical near-contact and interface regions. Beyond a yield point the materials (including that of the indenter[31]) are taken to deform according to a critical shear stress condition, with a bilinear constitutive uniaxial stress–strain relation $\sigma(\varepsilon)$:

$$\sigma = E\varepsilon \qquad (\sigma \leq Y) \quad , \qquad (1a)$$

$$\sigma = Y + \alpha(\varepsilon E - Y) \qquad (\sigma \geq Y) \quad . \qquad (1b)$$

Here E is Young's modulus, Y the uniaxial yield stress in compression, and α a dimensionless strain-hardening coefficient in the range $0 \leq \alpha \leq 1$ ($\alpha = 0$, fully plastic; $\alpha = 1$, fully elastic). The indenter is loaded incrementally onto the specimen, and contact radius a is evaluated stepwise as a function of load P, enabling generation of an indentation stress–strain curve. Values of E, Y, and α are then adjusted to match indentation stress–strain data.[33]

The results of such matches for our constitutive coating and substrate materials are included as the solid curves in Fig. 12, assuming the adhesive as part of the polycarbonate substrate. Parameters used in these fits are listed in Table I.

With these parameter adjustments we may evaluate the prefracture tensile stresses in the coating at any specified load P, for any specified thickness d. These stresses pertain to the initiation of first cracking—i.e., to glass surfaces with just upper *or* lower surfaces abraded. We investigate maxima in the radially directed principal tensile stresses σ_{11} normal to the outer C cracks on the upper surface and the hoop tensile stress σ_{22} normal to the M cracks at the lower surface. Figure 13 plots these stresses as a function of load P, for a representative thickness $d = 500$ μm within the intermediate range. Note the near-linear relations between σ and P, which contrasts with $\sigma \propto P^{1/3}$ for Hertzian contact fields[23] (Appendix). The horizontal dashed line in this figure represents the bulk glass strength $\sigma_F = 110$ MPa. Then, according to a critical stress condition for failure, the vertical dashed lines at the intersection points $\sigma = \sigma_F$ represent the critical loads P_c for crack initiation. Evaluations of $P_c(M)$ and $P_c(C)$ over the full intermediate d range enable us to generate the solid curves in Fig. 9 for comparison with the experimental P–d data.

Figure 14 plots the radial distribution of the σ_{11} surface stresses at $P = P_c$ (C) for the same coating thickness $d = 500$ μm as represented in Fig. 13. From plots of this kind we determine the location of the C-crack maximum surface stress as a function of thickness. Again, the solid curve in Fig. 10 is generated in this way.

Figure 15 plots contours of (a) σ_{11} and (b) σ_{22} tensile stresses at representative coating thickness $d = 500$ μm within the intermediate region, evaluated at the respective critical loads P_c (C) $= 320$ N and $P_c(M) = 28$ N to initiate C and M cracking. The σ_{11} stress contours in Fig. 15(a) are well spread out along the upper coating surface, with maximum distant from the contact circle,
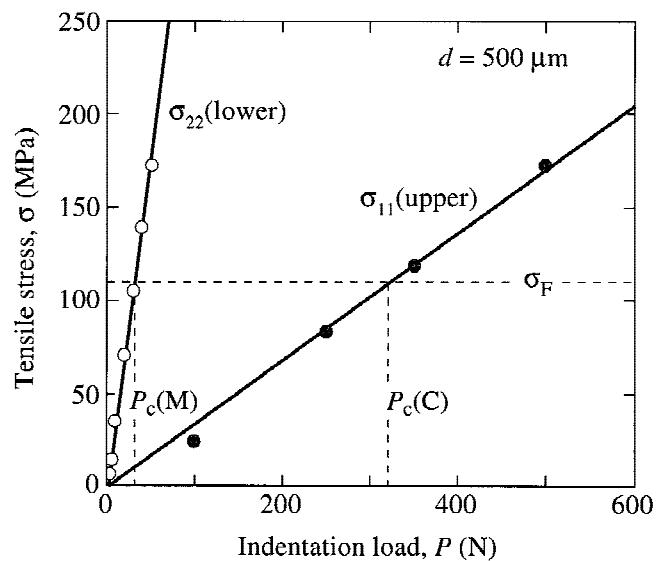
TABLE I. Material parameters in constitutive relation Eq. 1 for bulk coating and substrate materials represented in Figs 13–15.

Material	Young's modulus E (GPa)	Poisson's ratio ν	Yield stress Y (GPa)	Strain-hardening coefficient α
Soda-lime glass	70.0	0.22	⋯	1
Polycarbonate	2.35	0.35	0.10	0.25
Tungsten carbide	614	0.22	6.0	0.10

FIG. 13. Plot of tensile stresses σ_{11} on upper and σ_{22} on lower surfaces of glass coatings as function of load P, for thickness $d = 500$ μm, with WC indenter radius $r = 3.96$ mm. When σ equals the bulk strength σ_F of the abraded glass (horizontal dashed line), cracks are assumed to initiate at load $P = P_c$ (vertical dashed lines).

accounting for the wide radius of the C cracks. (Note, however, that the σ_{11} stresses are greatest at the lower surface, consistent with preinitiation of the M cracks.) Similarly, the σ_{22} contours in Fig. 15(b) are well spread
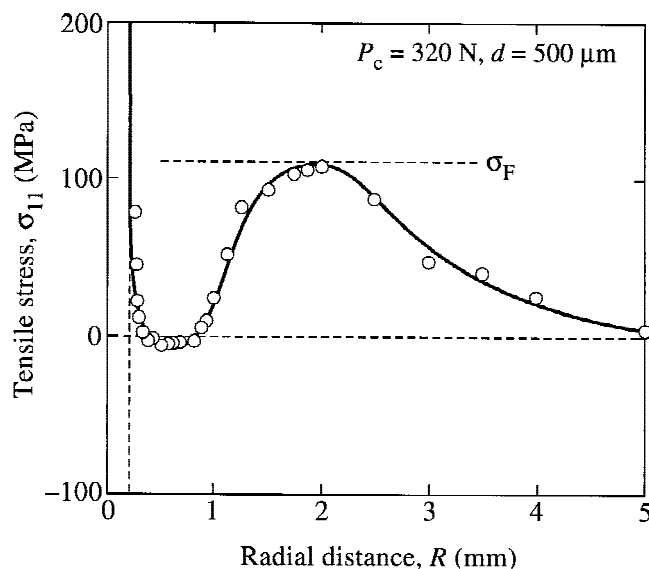

FIG. 14. Plot of tensile stresses σ_{11} on upper surface of glass coating, thickness $d = 500$ μm, at critical load $P_c(C) = 320$ N for initiation of circumferential cracks, with WC indenter radius $r = 3.96$ mm. Data points are FEM evaluations. Note location of maximum well outside contact circle (vertical dashed line).

(a)
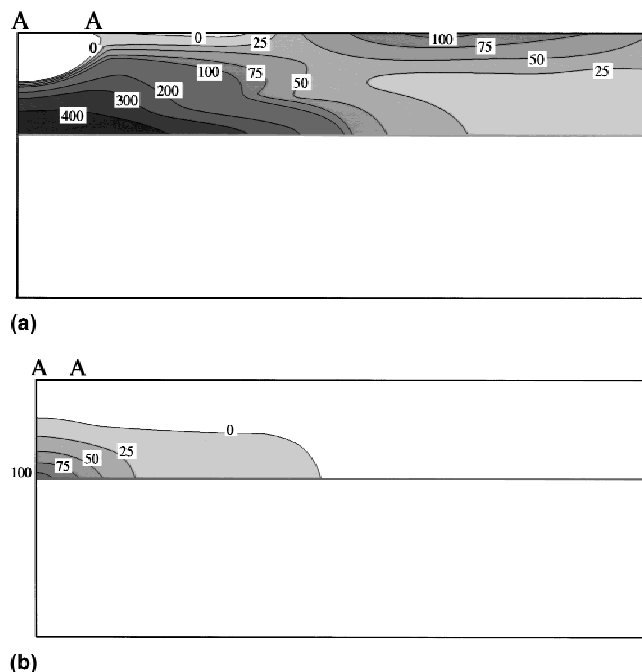

(b)

FIG. 15. Contours of principal tensile stresses (shaded areas) in glass coating, thickness $d = 500$ μm, on polycarbonate substrate, with WC indenter radius $r = 3.96$ mm, at critical loads: (a) σ_{11} stresses, $P_c(C) = 320$ N; (b) σ_{22} stresses, $P_c(M) = 28$ N. Stresses are in MPa, and AA denotes contact radius.

out along the lower coating surface, with maximum along the contact axis. It is interesting that these latter contours resemble the shape of the M cracks—note that the σ_{22} contours do not extend to the upper surface, consistent with the observed M-crack subsurface confinement. The σ_{11} surface and σ_{22} subsurface maxima in these plots correspond closely to the bulk glass strength 110 MPa. Away from the near-contact region, the stress field somewhat resembles a flexing plate with remotely clamped edges.

V. DISCUSSION

We have examined a range of transverse fracture modes in a model brittle coating system from contacts with hard spheres. Our choice of transparent constituent materials for both coating (soda-lime glass) and substrate (polycarbonate) enables *in situ* observation of the entire crack evolution. The modulus mismatch between the two materials is conveniently large, favoring the proliferation of a wide variety of crack systems in different regions of glass coating thickness. The bonding between coating and substrate is sufficiently strong as to preclude delamination fracture. In this work we have treated coating thickness as our key variable, investigating the changing crack patterns over a broad range, $d = 20$ μm to 5.6 mm, relative to a sphere radius $r = 3.96$ mm. Of greatest interest here is the "intermediate" thickness range, 50 μm $\lesssim d \lesssim 2$ mm ($0.013 \lesssim d/r \lesssim 0.5$), bridging the gap between limiting cases of the monolith at the high end and the thin film at the low end. Within this intermediate region the coating stress field takes on some of the character of a flexing plate. The cracks are of two kinds: median–radial M cracks, which initiate at the lower coating surface along the contact axis; circumferential C cracks, which initiate at the upper coating surface outside the contact circle. For thick coatings, 2 mm $\gtrsim d$ ($d/r \gtrsim 0.5$), the C cracks initiate in the conventional Hertzian near-cone geometry; for thin coatings, $d \lesssim 50$ μm ($d/r \lesssim 0.013$), the M and C cracks persist but are highly localized about the contact.[29]

The present *in situ* observations reveal some new aspects of crack evolution in systems where elastic (or, in nonlinear systems, plastic) mismatch is large. It is demonstrated that M cracks can be dominant over a wide range of coating thicknesses. This class of cracks has been previously reported,[2,3,5,8–10,34] but the morphology has not been hitherto systematically investigated as a function of coating thickness. In our system the M cracks extend laterally and upward from the lower interface, contradicting any presumption of upper surface initiation.[16] Indeed, the M cracks may remain entirely confined to the subsurface throughout their evolution. Such cracks may therefore pass unnoticed in routine surface inspections of damaged coatings, particularly in

opaque materials, making the prediction of imminent failure difficult. C cracks generally initiate at higher loads than M cracks in our system, although they can form first when the flaw state on the upper surface is substantially more severe than that on the lower surface. In the latter case the ring crack radius may extend 1 order of magnitude or more beyond the contact radius, especially at the upper end of the intermediate coating thickness range. When the flaw states of the two coating surfaces are similar, the critical loads for the C cracks are reduced by the preceding M-crack initiation, again with a widening differential at the upper end of the thickness range.

How general are the conclusions drawn from the observations on our large-mismatch coating–substrate system? Clearly, as the mismatch is reduced the behavior should tend toward that of a monolithic body, i.e., formation of conical surface C cracks in favor of subsurface M cracks. Nevertheless, proliferation of M cracks has been observed in bilayers with much lower elastic mismatch,[3] especially in systems in which the substrate deforms plastically beyond some yield stress.[2,5,6,9,10] The role of plastic deformation in reducing substrate compliance is particularly well demonstrated in glass/glass–ceramic systems, with near-identical elastic modulus in the two constituents but substantially lower yield stress in the glass–ceramic[5]—there, M cracks still precede C cracks. Accordingly, we may expect the M-crack mode to continue to play a primary role in many practical coating systems, e.g., cutting tools, teeth, and dental crowns, as long as the underlayer remains more compliant than the overlayer.[32,34]

Of central interest in the present study is the functional dependence of the critical loads P_c for the M and C cracks on coating thickness d, Fig. 9. It is these values that quantify the capacity of the coating system to operate in potentially damaging contact environments. The data in Fig. 9 confirm the M crack as the primary fracture mode over most of the thickness range, supplanting conventional cone fracture in monolith or thick-coating materials. The solid curves in this figure, evaluated from FEM tensile stress calculations in conjunction with a bulk strength condition for fracture, fit the first-fracture P_c–d data trends for both M and C cracks in the intermediate thickness range, within the scatter in data. It is not surprising that a critical stress condition should apply to reasonable approximation in this region, given the strong resemblance of the stress fields in the coating (at least remote from the contact) to that of a flexing plate at $d = 500$ μm in Fig. 15 and the corresponding linear relation between σ and P in Fig. 13. (In this context, recall that it is in flexure that the bulk strengths of brittle materials are measured.) It is interesting to consider the observed dependence $P_c \propto d^{1.75}$ for M cracks in Fig. 9 with the elasticity solution for a stiff circular plate

(modulus E) of thickness d on a soft foundation (stiffness k) with center load uniformly distributed over contact radius a:[35]

$$\sigma = \beta(P/d^2) \log(Ed^3/ka^4) \quad . \tag{2}$$

Here β is constant. Hence for $\sigma = \sigma_F = $ constant we expect $P_C \propto d^n$, with $n < 2$, allowing for a weak dependence on d in the logarithmic term, i.e., not inconsistent with exponent $n \approx 1.75$.

A comment on the generality of the critical stress condition for crack initiation, widely used in the solid mechanics literature, is in order here. Use of such a condition implies that the applied stress field is essentially uniform over the area of the starting flaw, a state that is strictly attained only in ideal tensile tests. In common stress fields this requirement is only a first approximation and can be violated altogether. It certainly breaks down in the case of Hertzian cone fracture in monoliths or very thick coatings (see Appendix), because of highly concentrated negative stress gradients just outside the contact circle where the initiation occurs—the values of P_c for C cone cracks are then much higher than predicted from a simple critical stress condition, especially for smaller indenters where the gradients are accentuated.[21–24,36,37] A critical stress condition must also be expected to underestimate P_c in the case of very thin films, where the thickness diminishes toward the size of the starting flaws (cf. $d < 50$ μm in the thin film region of Fig. 9 with the estimated flaw size $c_f \approx 10$ μm for our abraded glass) owing to stress falloff across the coating section.

Another interesting aspect of the coating fracture is the size of the surface circumferential C cracks in relation to the coating thickness d and sphere radius r. Accordingly, the data used to construct Fig. 10 are replotted in Fig. 16 as normalized crack dimension R_0/d versus normalized coating dimension d/r. In this figure the solid horizontal line at $R_0/d \approx 4$ through data for *outer* C cracks implies a self-similarity in the crack geometry relative to the coating geometry in this intermediate region, independent of contact geometry. The inclined dashed line of slope −1 (logarithmic coordinates) through a large portion of the data for the *inner* C cracks (except at 50 μm $d < 500$ μm) corresponds to a constant ring diameter $R_0/d \approx 0.075r/d$ (i.e., $R_0 \approx 300$ μm, independent of d), suggesting that the diminishing effect of a lower P_c at smaller d is effectively counterbalanced by the enlarging effect a more compliant sublayer. Of course, the curves in Fig. 16 are also dependent on the material modulus properties.

Finally, there are other issues in the crack evolution that remain to be fully explored in brittle coatings on soft substrates:

(i) *Residual contact stresses.* The coating cracks all form and extend during the loading half cycle. No ini-
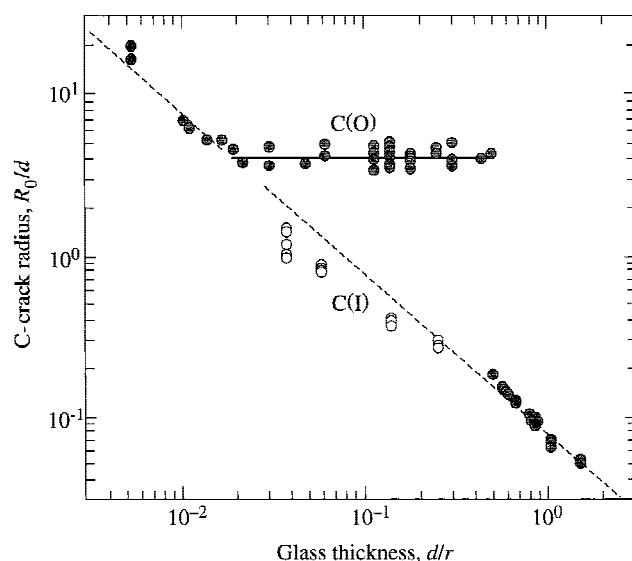
FIG. 16. Plot of normalized C-crack radius (outer O, inner I; see Fig. 1) as function of normalized coating thickness, for glass coating on polycarbonate substrate, with WC indenter radius $r = 3.96$ mm. Filled and unfilled symbols indicate first-fracture and subsequent-fracture events, respectively.

tiation or continued extension is observed during unloading, suggesting that residual stresses are not too important in our system. However, such stresses may be critical in systems with highly yielding substrates and sharp indenters,[16,38] especially in the evolution of delamination cracks at weak interfaces.[38]

(*ii*) *Fracture mechanics.* How do the newly initiated cracks extend as a function of load, i.e., what is the form of the $c(P)$ relations? The M and C cracks are seen to be highly stable (Figs. 2–5), making penetration through the coating difficult in high-mismatch bilayers. At higher loads, how do crack–crack interactions (e.g., Fig. 4) influence the mechanical response—e.g., how does the pre-existence of M cracks reduce P_c for the onset of C cracks at larger d values within the intermediate range in Fig. 9?

(*iii*) *Critical loads to failure.* We have measured P_c for first and subsequent cracking, but what are the critical loads at which these cracks ultimately penetrate through the coating and thereby signal failure of the system? Previous studies on coating systems with lesser modulus mismatch suggest that these loads can be high relative to the initial cracking loads, pointing to an inherent resilience and damage tolerance in these layer structures.[11]

(*iv*) *Flaw statistics.* As seen in Fig. 11, the critical loads to initiate M and C cracks in the intermediate thickness region are flaw sensitive. The preparation and service histories of coatings will be important issues in the responses of real coatings in practical applications. On the other hand, the high stability of the cracks in their fully developed form render the subsequent evolution to failure somewhat insensitive to surface flaw state.

REFERENCES

1. M.V. Swain and J. Mencik, Thin Solid Films **253,** 204 (1994).
2. L. An, H.M. Chan, N.P. Padture, and B.R. Lawn, J. Mater. Res. **11,** 204 (1996).
3. D.F. Diao, K. Kato, and K. Hokkirigawa, Trans. ASME J. Tribology **116,** 860 (1994).
4. A. Pajares, L. Wei, B.R. Lawn, N.P. Padture, and C.C. Berndt, Mater. Sci. Eng. **A208,** 158 (1996).
5. S. Wuttiphan, B.R. Lawn, and N.P. Padture, J. Am. Ceram. Soc. **79,** 634 (1996).
6. A.C. Fischer-Cripps, B.R. Lawn, A. Pajares, and L. Wei, J. Am. Ceram. Soc. **79,** 2619 (1996).
7. H.M. Chan, Ann. Rev. Mater. Sci. **27,** 249 (1997).
8. T.J. Lardner, J.E. Ritter, and G-Q. Zhu, J. Am. Ceram. Soc. **80,** 1851 (1997).
9. K.S. Lee, S. Wuttiphan, X.Z. Hu, S.K. Lee, and B.R. Lawn, J. Am. Ceram. Soc. **81,** 571 (1998).
10. K.S. Lee, S.K. Lee, B.R. Lawn, and D.K. Kim, J. Am. Ceram. Soc. **81,** 2394 (1998).
11. Y.G. Jung, S. Wuttiphan, I.M. Peterson, and B.R. Lawn, J. Dent. Res. **78,** 887 (1999).
12. K. Komvopolous, ASME J. Tribology **111,** 430 (1989).
13. P. Montmitonnet, M.L. Edinger, and E. Felder, ASME J. Tribology **115,** 15 (1993).
14. Y. Sun, A. Bloyce, and T. Bell, Thin Solid Films **271,** 122 (1995).
15. K.C. Tang, A. Faulkner, N. Schwarzer, R.D. Arnell, and F. Richter, Thin Solid Films **300,** 177 (1997).
16. K. Hayashi and F. Yuan, ASME J. Tribology **120,** 463 (1998).
17. S. Sen, B. Aksakal, and A. Ozel, Int. J. Mech. Sci. **40,** 1281 (1998).
18. H. Hertz, *Hertz's Miscellaneous Papers* (Macmillan, London, 1896), Chaps. 5 and 6.
19. J.P. Tillett, Proc. Phys. Soc. Lond. **B69,** 47 (1956).
20. F.C. Roesler, Proc. Phys. Soc. Lond. **B69,** 981 (1956).
21. F.C. Frank and B.R. Lawn, Proc. R. Soc. London **A299,** 291 (1967).
22. B.R. Lawn and T.R. Wilshaw, J. Mater. Sci. **10,** 1049 (1975).
23. B.R. Lawn, J. Am. Ceram. Soc. **81,** 1977 (1998).
24. F.B. Langitan and B.R. Lawn, J. Appl. Phys. **40,** 4009 (1969).
25. M.V. Swain and B.R. Lawn, Phys. Status Solidi **35,** 909 (1969).
26. F. Guiberteau, N.P. Padture, H. Cai, and B.R. Lawn, Philos. Mag. **A68,** 1003 (1993).
27. H. Cai, M.A. Stevens Kalceff, and B.R. Lawn, J. Mater. Res. **9,** 762 (1994).
28. T.R. Wilshaw, J. Phys. D: Appl. Phys. **4,** 1567 (1971).
29. M.R. Begley, A.G. Evans, and J.W. Hutchinson, Int. J. Solids Struct. **36,** 2773 (1999).
30. C.J. Culf, J. Soc. Glass Technol. **41,** 157T (1957).
31. A.C. Fisher-Cripps and B.R. Lawn, J. Am. Ceram. Soc. **79,** 2609 (1996).
32. S. Wuttiphan, A. Pajares, B.R. Lawn, and C.C. Berndt, Thin Solid Films **293,** 251 (1997).
33. A.C. Fischer-Cripps and B.R. Lawn, Acta Mater. **44,** 519 (1996).
34. S. Wuttiphan, Ph.D. Thesis, University of Maryland (1997).
35. S. Timoshenko and S. Woinowsky-Krieger, *Theory of Plates and Shells* (McGraw-Hill, New York, 1959), p. 275.
36. B.R. Lawn, *Fracture of Brittle Solids* (Cambridge University Press, Cambridge, U.K. 1993), Chap. 8.

37. S.K. Lee, S. Wuttiphan, and B.R. Lawn, J. Am. Ceram. Soc. **80,** 2367 (1997).
38. A. Pajares, L. Wei, B.R. Lawn, and C.C. Berndt, J. Am. Ceram. Soc. **79,** 1907 (1996).

APPENDIX: CRITICAL STRESSES IN THE HERTZIAN FIELD

In classical Hertzian contact with a sphere of radius r at load P the maximum tensile stress σ_m at the contact circle can be written[23]

$$\sigma_m = \tfrac{1}{2}\,(1 - 2\nu)(3E/4k)^{2/3}\,(P/\pi r^2)^{1/3} \quad , \qquad (3)$$

where $k = (9/16)[(1 - \nu^2) + (1 - \nu'^2)E/E']$, with E Young's modulus, ν Poisson's ratio, and the prime denoting the indenter material. Using the elastic constants for glass specimen and WC indenter materials in Table I, and inserting $P = P_c = 220N$ at $r = 3.96$ mm for our monolithic glass (horizontal dashed line in Fig. 9), we calculate $\sigma_m = 900$ MPa for the maximum tensile stress at cone crack initiation.

This value compares with the bulk glass strength $\sigma_F = 110$ MPa measured in our experiments, indicating a major breakdown in the critical stress condition for crack initiation from the near-contact zone.